Global NEST Journal, **28** (7), 08490
Available online: 14/08/2026

Evolution and Driving Mechanisms of Carbon Emissions in the Yangtze River Delta Demonstration Zone (1990-2025) Based on Land Use

Yuxun Zhang[a,b,c]*, Yunchun Ye[c,d] and Qinping Yu[c,d]

[a]College of Environment and Life Science, Weinan Normal University, Weinan 714000 China;
[b]Key Laboratory for Ecology and Environment of River Wetlands in Shaanxi Provincial, Weinan 714000 China;
[c]School of Environmental and Geographical Sciences, Shanghai Normal University, Shanghai 200234, China;
[d]Yangtze River Delta Urban Wetland Ecosystem National Field Observation and Research Station, Shanghai 200234, China

*Correspondence e-mail: zhangshangxun@wnu.edu.cn

Abstract

Carbon emissions are critical to sustainable development, with land use and land cover change (LUCC) being a key influencing factor. However, clarifying the variations in land-use carbon emissions driven by multiple factors remains challenging. As an ecological pilot in China's Yangtze River Delta (YRD), the YRD Demonstration Zone provides an ideal case for studying land-use carbon dynamics. This study analyzed the evolution characteristics and drivers of land-use carbon emissions in the zone using Landsat imagery from 1990 to 2025 and machine learning algorithms. The land-use classification model achieved an accuracy of 0.93, with transferable accuracy averaging 0.91. Notable transitions included persistent conversion of paddy fields to terrestrial vegetation and impervious surfaces, while wetlands remained stable. Carbon accounting revealed increases in both sinks and sources, with net emissions remaining source-dominated. Using the LMDI (Logarithmic Mean Divisia Index) model and collinearity analysis, main drivers of net emissions were identified and ranked as: economic development > carbon sink pressure > industrial-ecological balance > regional population > economic structure. This study clarifies how land-use transitions affect regional carbon balance, offering a scientific basis for low-carbon development and sustainable land management in the YRD.

Keywords: Land use; Machine learning; Yangtze River Delta Demonstration Zone; LMDI; Driving factors.

OPEN ACCESS

Received: 05/03/2026,

Accepted: 28/07/2026,

Available online: 14/08/2026

Graphical abstract

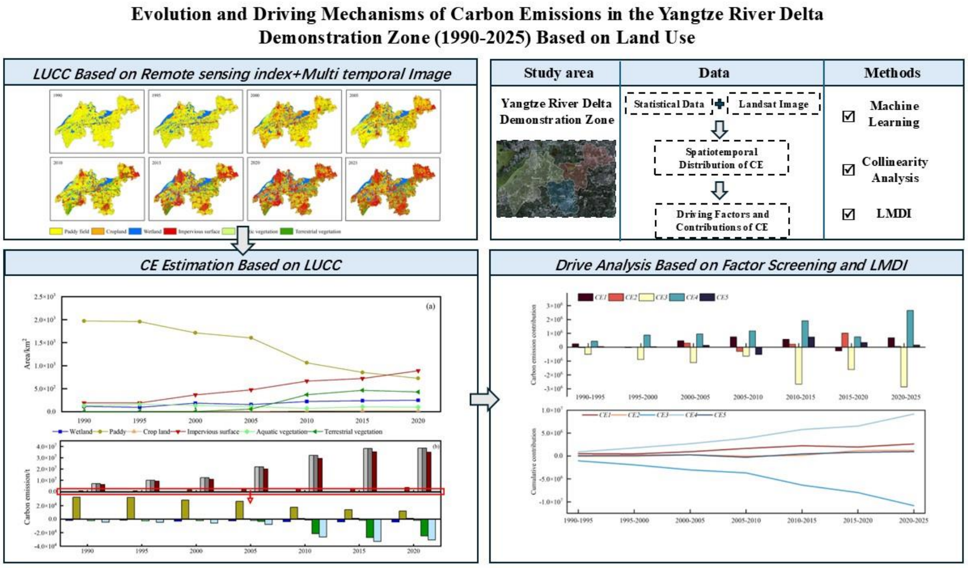

1. Introduction

Land use and land cover change (LUCC) significantly influences material cycling and energy flow in terrestrial ecosystems, making it a vital aspect of global environmental change research (Fu *et al.*, 2015; Song *et al.*, 2018). In diverse environmental contexts, shifts in land use intensity further influence ecosystem structure and function, with impact mechanisms showing marked regional variability (Gomes *et al.*, 2021; Xie *et al.*, 2022; Zheng *et al.*, 2022). Specifically in carbon cycling, LUCC acts as a key driver of regional carbon emission and sequestration capacity changes (Beillouin *et al.*, 2022; Bogale *et al.*, 2024). In 2020, China explicitly set the "dual-carbon" goals, aiming to achieve sustainable and high-quality development (Jia *et al.*, 2022; Wu *et al.*, 2023). The substantial changes in land use and carbon emissions throughout prolonged urbanization have notably affected regional sustainable development. Understanding land use change and its impact on carbon emissions is crucial for promoting regional sustainable development.

Carbon emission estimation methods primarily encompass the IPCC approach (Köne & Büke, 2019), estimation using nighttime light data (Sun *et al.*, 2023; Wang *et al.*, 2024), and carbon emission calculation based on land use types (Tian *et al.*, 2021; P. Wang *et al.*, 2025). Among these, the carbon emission calculation method based on land use types can directly reflect the impact of different land-use patterns on carbon emissions. Carbon emissions from land use are classified into direct and indirect emissions (Tian *et al.*, 2021; Zhang *et al.*, 2022). Direct carbon emissions are greenhouse gases emitted into the atmosphere from physical, chemical, and biological processes during land-use activities. Indirect carbon emissions are those generated in other land-related processes because of land-use changes or management activities. Estimating land-use carbon emissions requires obtaining relevant land-use data and its changes.

Traditional land use classification methods heavily rely on manual visual interpretation. Although widely applied, these methods are hampered by issues such as high subjectivity and low efficiency. With the rapid development of information technology (Hou *et al.*, 2025), machine learning has emerged as the primary approach for remote sensing-based land use classification (Aryal *et al.*, 2023; Chaturvedi & de Vries, 2021), including ANN (Li *et al.*, 2018; Liu *et al.*, 2025) and SVM (Huang *et al.*, 2010). Operating under standardised protocols (Hou & Liu, 2024), these algorithms demonstrate strong robustness in identifying complex land cover types such as wetlands and urban areas. Furthermore, high-precision monitoring of large-scale, long-term land use dynamics can be achieved by integrating multi-source remote sensing data with machine learning (DeLancey *et al.*, 2020).

The Yangtze River Delta (YRD) is a globally influential urban agglomeration and a core area for China's economic growth and urbanization. However, intensive human activities have caused multiple environmental pressures—wetland loss, ecological degradation, groundwater overexploitation, and air pollution (Lin *et al.*, 2021; Lu *et al.*, 2022; Shang *et al.*, 2021; Sun *et al.*, 2021). The creation of the Yangtze River Delta demonstration zone for green and integrated ecological development serves as a crucial initiative for advancing regional coordination and green transformation. The demonstration zone aims to harmonise human-land relationships, alleviate ecological-economic conflicts, and provide a model for sustainable development across larger regions (Gao *et al.*, 2024; Ren *et al.*, 2024). However, the mechanisms linking land use carbon emissions to sustainable development in this region have been relatively underexplored.

This study conducts a carbon emission accounting for the YRD Demonstration Zone over the period 1990 ~ 2025, based on statistical data and machine learning approaches. Drawing upon the accounting results, the driving factors underlying carbon emissions in the region are examined in detail. The study is designed to achieve three primary objectives. First, a transferable hybrid classifier is developed to enable cross-sensor calibration of the land-use model using time-series samples, thereby facilitating high-precision extraction of long-term land-use information. Second, the LMDI (Logarithmic Mean Divisia Index) decomposition framework is refined by incorporating a VIF-based collinearity pre-screening step, which mitigates the interference caused by inter-factor correlations in contribution estimation and moves beyond the conventional emphasis on economic and demographic variables. Third, the study identifies the dominant driving factors of net carbon emissions in the YRD Demonstration Zone and establishes their relative influence, providing a scientific basis for the formulation of differentiated low-carbon development strategies and the optimisation of territorial spatial planning. Ultimately, this research offers a reference for low-carbon development and sustainable land management in the YRD Demonstration Zone and beyond.

2. Materials and Methods

2.1. *Study area*

The demonstration zone (N 30.75° ~ 31.30°, E 120.36° ~ 121.32°) lies in a typical subtropical monsoon climate zone, featuring distinct seasons, mild humidity, abundant rainfall, and annual temperatures averaging 16 ~ 18°C. The YRD Regional Integration Development Plan Outline, announced in May 2019, designated the demonstration zone to include Qingpu District (Shanghai), Wujiang District (Jiangsu), and Jiashan County (Zhejiang). The total regional area spans approximately 2413 km² (**Figure 1**).

2.2. *Remote sensing data*

This study utilises Landsat satellite remote sensing imagery as the main data source, specifically incorporating data from Landsat 8 OLI and Landsat 5 TM sensors (**Table 1**). The spectral bands employed encompass blue, green, red, near-infrared (NIR), and shortwave infrared (SWIR) ranges, each with a spatial resolution of 30 meters. These bands offer significant advantages in vegetation identification, wetland extraction, and land cover classification. They facilitate long-term analysis of land use and land cover changes using time-series data.

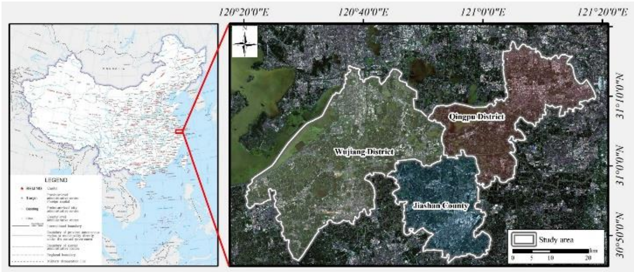

Figure 1. Location of the YRD demonstration zone

Landsat data from 1990 to 2025 were selected, with the images sourced from the USGS portal (https://glovis.usgs.gov/). These images had been systematic geometric correction by USGS. To obtain accurate land use/cover information, preprocessing focuses on radiometric calibration and atmospheric correction. In ENVI 5.3, the Radiometric Calibration tool converted Digital Number (DN) values to apparent radiance (calibration type: Radiance; coefficient: 0.10). Subsequently, the FLAASH module conducted atmospheric correction—automatically matched atmospheric models by imaging time, setting aerosol model to Rural, and visibility to 40 km. This eliminated scattering/absorption effects, yielding true surface reflectance.

Table 1. Band (μm) of Landsat 8/OLI and Landsat 5/TM Sensors.

	Coastal	Blue	Green	Red	NIR	SWIR 1	SWIR 2	Pan	Cirrus
Landsat-8/OLI	0.433～0.453	0.450～0515	0.525～0.600	0.630～0.680	0.845～0.885	1.560～1.660	2.100～2.300	0.500～0.680	1.360～1.390
Landsat-5/TM	——	0.450～0.520	0.520～0.600	0.630～0.690	0.760～0.900	1.550～1.750	2.080～2.350	——	——

Table 2. Remote sensing image data sources

Year	Data source	Imaging time	
		Image I	Image II
1990	Landsat5/TM	1990-05-10	1990-10-08
1995	Landsat5/TM	1994-05-12	1995-10-15
2000	Landsat5/TM	2000-06-13	2000-11-04
2005	Landsat5/TM	2005-06-04	2005-10-17
2010	Landsat5/TM	2010-05-24	2010-10-31
2015	Landsat8/OLI	2015-05-22	2015-10-13
2020	Landsat8/OLI	2020-05-19	2019-11-09
2025	Landsat8/OLI	2025-06-18	2024-11-06

Seamless Mosaic was used to merge same-date images, which were then clipped using the vector boundary of the demonstration zone. For each time window, the two remote sensing images were selected based on the principle of minimising cloud cover within similar months. The data at five-year intervals from 1990 to 2025 constitute the time-series dataset for land use classification in this study (imaging time: **Table 2**).

2.3. *Remote sensing index*

Remote sensing indices are numerical values derived from linear/nonlinear combinations of surface reflectance across multiple wavelengths. In general, these indices provide specific indicators for target features (Galvanin *et al.*, 2014; She *et al.*, 2015; Tesfaye & Awoke, 2021). They are closely related to various surface parameters, which enables effective ground information extraction with strong interference resistance. These indices also mitigate influences from solar elevation, topographic relief, and atmospheric conditions. To achieve classification of multiple wetland types, the study selected remote sensing indices that included the SWIR band, which is sensitive to water body changes. Based on Landsat band characteristics, this study selected three indices: Normalised Difference Vegetation Index (NDVI) and two different types of Normalised Difference Water Index (NDWI). Details and formulas are provided in **Table 3**.

Table 3. Remote sensing index and expression.

Remote sensing index	Expression	Reference
NDVI	(Nir-Red)/(Nir+Red)	(Tucker, 1979)
NDWI 1	(Nir-SWIR1)/(Nir+SWIR1)	(Gao, 1996)
NDWI 2	(Nir-SWIR2)/(Nir+SWIR2)	(Gao, 1996)

2.4. *Land use classification*

Given the extensive distribution and diverse types of wetlands in the study area, this study integrates the Ramsar Convention wetland classification system with China's National Wetland Resources Survey and Classification Standards. Combining land use characteristics of the YRD demonstration zone with the identifiability of remote sensing imagery, the wetland system is categorised into natural wetlands and constructed wetlands. Natural wetlands consist of open water bodies and aquatic vegetation areas, while constructed wetlands primarily refer to paddy fields. Non-wetland types encompass impervious surface, cropland, and terrestrial vegetation. In this study, 'total wetland' includes natural wetlands (i.e., wetland and aquatic vegetation areas) and artificial wetlands (i.e., paddy fields).

2.4.1. *Classification dataset*

This study utilised 2020 GF-2/PMS (2 m spatial resolution) land use data. These data were obtained through visual interpretation of land use results for the study area in that year. Based on the visual interpretation results, multiple sampling points were selected using the 'Create Random Points' tool in ArcGIS to construct training samples for the study area. A training sample library was established using two images from 2020, ensuring that the sample size for each land cover type was no less than 1,000. Data from six bands (blue, green, red, near-infrared, short-wave infrared) and three remote sensing index layers (NDVI, NDWI 1, NDWI 2) were input. The standard deviations of the three remote sensing index layers were calculated using the moving average method to construct Dataset 1. The samples in Dataset 1 were divided into training data and validation data at a ratio of 3:1.

Table 4. Sample dataset of land use classification model

	Wetland	Paddy fields	Impervious surface	Terrestrial vegetation	Cropland	Aquatic vegetation	Year
Dataset 1	2282	1962	2149	1155	1046	1123	2020
Dataset 2	550	580	548	566	568	596	1990
	595	503	582	595	556	567	1995
	529	504	506	552	523	547	2000
	548	536	514	516	550	530	2005
	592	505	593	544	559	587	2010
	542	545	593	535	572	555	2015
	532	509	520	521	526	538	2020
	551	510	523	511	502	542	2025

Given the relatively long-time span of the remote sensing images used for classification, there may be adaptation issues when applying the model to data from different types of sensors during the model transfer process. Consequently, collaborative calibration of multi-source sensor data is essential. However, since the operational cycles of Landsat 8 and Landsat 5 satellites do not overlap, their reflectance data cannot be directly converted. To address this issue, the study randomly collected no fewer than 500 samples from each image in the remaining years to construct Dataset 2. Dataset 2 was used to calibrate errors in the time-series data and analyze their distribution characteristics. **Table 4** presents Datasets 1 and 2.

2.4.2. *Classification model and accuracy evaluation*

The classification model consists of two modules. Module I utilises the SVM algorithm to build a pre-trained model with Dataset 1. Module II functions as a data optimization and adjustment unit, refining the model using Dataset 2 through the Backpropagation Neural Network (BPNN) algorithm. The structure and data flow of the classification model are shown in **Figure 2**.

Built on SVM, Module I first pre-trains with relevant data and then feeds the results, along with Dataset 2, into Module II for optimization. During Module II's optimization, the SVM kernel function from Module I is set to the Radial Basis Function Gaussian (RBF). In each iteration, the SVM's Gamma parameter is fine-tuned between 0.100 and 0.300 in increments of 0.001. Simultaneously, Module I's output undergoes 1,000 training iterations to achieve a pre-trained model with optimal accuracy. In Module's repeated fitting, only the hidden layer's neuron count is adjusted, keeping the number of hidden layers constant. The sigmoid function is selected as the activation function, and the step size for neuron variation is set to 1. Ultimately, through training and optimization in both modules, the optimal classification model is obtained. This study employs the Markov transition matrix and Kappa coefficient to calculate classification accuracy, and the formula is as follows:

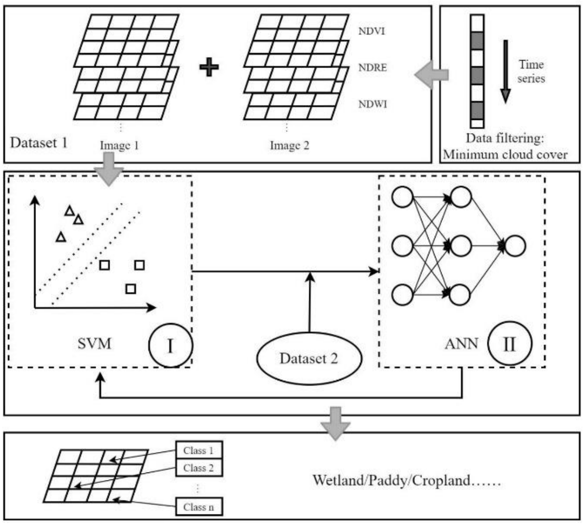

Figure 2. Classification model and data flow

$$\begin{array}{cc} \begin{array}{c} a_1 \\ \vdots \\ a_i \end{array} & \begin{bmatrix} p_{11} & \cdots & p_{1j} \\ \vdots & \ddots & \vdots \\ p_{i1} & \cdots & p_{ij} \end{bmatrix} = P \\ & \begin{array}{ccc} a_1 & \cdots & a_j \end{array} \end{array} \quad (1)$$

Each element in the transition matrix should meet the following conditions:

$$0 \leq P_j \leq 1 \quad (2)$$

$$\sum_{j=1}^{n} P_{ij} = 1 \quad (3)$$

P_{ij} represents the probability of a land cover type transitioning from type *i* to type *j*, and *n* is the total number of land cover types.

$$\text{Kappa} = (p_0 - p_e)/(1 - p_e) \quad (4)$$

p_0 is defined as the ratio of the sum of correctly classified sample counts for each class to the total number of samples, representing the overall classification accuracy; p_e is defined as the sum of the products of the actual sample count and the predicted sample count for each class, divided by the square of the total number of samples.

2.5. *Carbon emission*

For carbon emissions associated with urban impervious surfaces,the core statistical foundation draws on officially published energy consumption datasets released by local administrative authorities. For data entries not directly retrievable from existing statistical systems, this research adopts economic or demographic proportional indicators to complete targeted estimation and data supplementation. Specifically, the annual total energy consumption (measured in tonnes of standard coal equivalent) for the full administrative jurisdictions of Shanghai, Jiangsu Province and Zhejiang Province was extracted from their respective provincial statistical yearbooks. To downscale these provincial datasets to the YRD Demonstration Zone level, the ratio of the demonstration zone's GDP to the corresponding provincial GDP was applied as a proxy indicator. For estimating carbon emissions from different land types such as farmland, terrestrial vegetation, and wetlands, this study adopts the direct carbon emission coefficient method The specific estimation formula presented as follows：

$$E = \sum e_i = \sum S_i \times \delta_i \quad (5)$$

E represents the estimated total land use carbon emissions; e_i is the carbon emissions from the *i*-th land use type; S_i is the area of the corresponding land use type; δ_i is the carbon emission coefficient per unit area for the *i*-th land use type; and *i* denotes different land use types; Positive values in the calculation result indicate carbon emissions, while negative values indicate carbon absorption or sequestration.

Carbon sink/source and emission coefficients for different land use types are based on existing research (Cai *et al.*, 2005; Duan *et al.*, 2008; Shen *et al.*, 2024). The emission factors for each land type are as follows: -0.0581 kg/m^2 •a (Terrestrial vegetation), 0.0497 kg/m^2 •a (Cropland), 0.01644 kg/m^2 •a (Paddy), and 0.01682 kg/m^2 •a (Wetland and Aquatic vegetation). For carbon emissions related to urban areas, the statistical basis is the energy consumption data published by the government. Due to the absence of data for some years, the study employs economic or population proportion indicators for estimation and completion.

2.6. *Analysis of Driving Factors*

2.6.1. Screening of Driving Factors

This study utilised collinearity analysis with the Variance Inflation Factor (*VIF*) to identify factors influencing net carbon emissions (*C*) in the demonstration zone. The factors considered were Gross Regional Product (*GDP*), secondary industry output (*SIO*) and proportion (*PSI*), energy consumption (*EC*), construction land area (*CLA*), total carbon emissions (*TCE*), wetland area (WA), terrestrial vegetation area (*TVA*), and total regional population (*TRP*). A higher *VIF* value signifies greater collinearity among the independent variables. Collinearity is considered insignificant when *VIF* is less than 5, moderate when *VIF* is between 5 and 10, and severe when *VIF* is 10 or higher. The calculation formula for *VIF* is presented as follows:

$$VIF_i = \frac{1}{1-R^2_{\ i}} \tag{6}$$

$$R^2 = 1 - \frac{\Sigma\left(y_i - y_i\right)^2}{\Sigma\left(y_i - \bar{y}\right)^2} \tag{7}$$

$R^2_{\ i}$ represents the coefficient of determination of the regression model where the *i*-th independent variable is regressed on the other independent variables. Y_i is the actual observed value, and y_i is the predicted value by the model.

2.6.2. LMDI model

The LMDI method decomposes changes in a target variable, like total carbon emissions, into the contributions of various driving factors such as economic scale, industrial structure, and energy efficiency, allowing for the quantification of each factor's impact on the overall change. This study utilised LMDI to examine the factors influencing carbon emissions in demonstration zone.

$$C = \frac{C}{E_1} \times \frac{E_1}{E_2} \times \ldots \times E_n = CE_1 \times CE_2 \times \ldots \times CE_i \tag{8}$$

In the formula, *C* represents the net carbon emissions from land use; *Ei* denotes the different driving factors affecting carbon emissions in the demonstration zone.

$$\Delta C = \Delta C^t - \Delta C^0 = \Sigma \Delta CEi \tag{9}$$

In the formula, C_0 is the land use carbon emissions in the base year, *Ct* is the land use carbon emissions in the final year, and Δ*i* is the land use carbon emission effect resulting from the development of several decomposed factors.

3. Results and Analysis

3.1. *Classification model*

The classification model achieved an overall classification accuracy of 0.93 (Results based on the year of visual interpretation data). The matrix of the classification results is shown in **Table 5**. After migrating the model to observation windows of different years for classification applications, the average accuracy reached 0.91 (**Figure 3**). Since the training samples were derived from Landsat 8/OLI image data in 2020, the classification accuracy was relatively high in 2015 when Landsat 8/OLI data was also used.

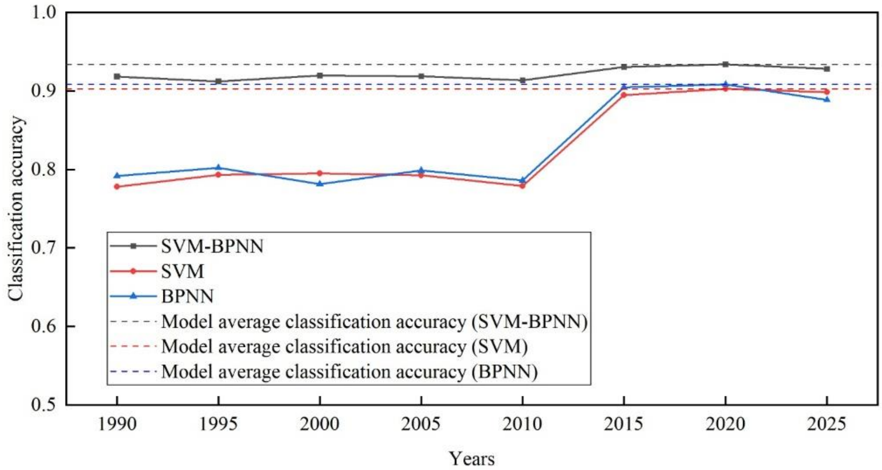

Figure 3. Changes in the accuracy of the classification model.

Table 5. Classification accuracy of training dataset

	Wetland	Paddy fields	Impervious surface	Terrestrial vegetation	Cropland	Aquatic vegetation	Total
Wetland	1975	75	0	0	0	32	2082
Paddy fields	194	1820	7	41	12	16	2090
Impervious surface	0	3	2101	15	2	0	2121
Terrestrial vegetation	0	45	38	1094	3	0	1180
Cropland	0	19	3	5	991	0	1018
Aquatic vegetation	113	0	0	0	0	1075	1188
Total	2282	1962	2149	1155	1046	1123	9717

The classification results from 1990 to 2010 were generated by migrating the model to Landsat 5/TM images, with accuracy ranging from 0.90 to 0.92. Based on the **Table 5** and Eq. 4, the overall Kappa coefficient for the classification in 2020 was calculated as 0.9169 in this study. When the model was transferred to other years, the mean Kappa across all time steps was 0.8922, confirming its good temporal generalisation ability. Although slightly lower than the classification accuracy in 2015 and 2025, these accuracies remained at a relatively high level. The classification results provided essential data for estimating land use carbon emissions and analyzing driving factors in this study. Using the same single-year dataset and hyperparameter optimisation, two independent classifiers (SVM and ANN models) were trained. The accuracies of these two classifiers were 0.90 and 0.91, respectively, slightly lower than the accuracy of the model corrected with time-series samples. After transferring to the remaining years, the mean accuracies of the SVM and ANN models were 0.82 and 0.83, respectively. By contrast, the SVM-BPNN hybrid model offered a favourable trade-off between accuracy and transferability. The reduction in classification accuracy may have arisen from uncorrected sensor discrepancies between Landsat 5 and Landsat 8.

3.2. *Land use in the demonstration zone*

In terms of area proportion, the land use monitoring results of the demonstration zone in 2025 (Fig. 4) reveal that the land use types in this region, ranked from high to low, are as follows: impervious surface > paddy field > wetland > terrestrial vegetation > aquatic vegetation > cropland.

Impervious surfaces constitute 36.94 % of the demonstration zone's total area. They are relatively concentrated in three districts/counties, with a small portion scattered along the lakeshores and the banks of main roads. Natural wetlands comprise about 20 % of the demonstration zone's total area. These wetlands exist in the form of lakes and rivers of varying sizes, with relatively concentrated distribution in the western and northern regions. The main water bodies include East Taihu Lake and Dianshan Lake. Aquatic vegetation is primarily distributed along the shoreline of East Taihu Lake. Paddy fields are mainly concentrated in Wujiang District and Jiashan County. Terrestrial vegetation covers 19.86 % of the area, primarily situated in the southwestern region of the demonstration zone and the downstream section of the Taipu River. Given its strong carbon sink capacity, its large-scale distribution plays a positive role in reducing carbon emissions in the demonstration zone.

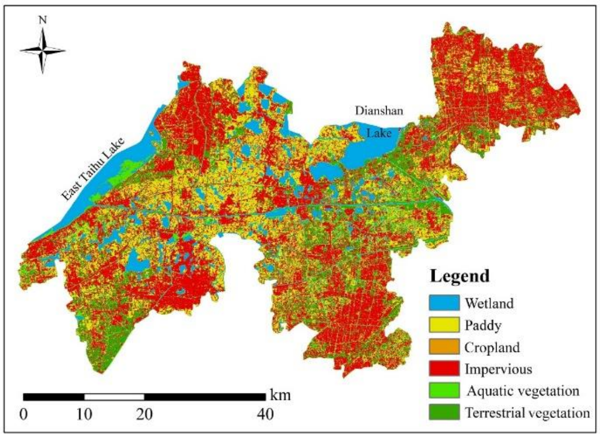

Figure 4. Land use in the YRD demonstration zone in 2025

Analysis of land use statistics revealed that impervious surfaces are the main contributors to carbon emissions, totaling around 4.18×10^7 t. Spatially, carbon sources and sinks in the demonstration zone displayed an interwoven distribution.

The demonstration zone's net carbon emissions were approximately 3.80×10^7 t, with terrestrial vegetation serving as the primary carbon sink, sequestering about 2.78×10^4 t. Although natural wetlands cover an area of 348.57 km², the carbon sink rate of the main lake area in the Taihu Lake Basin (16.82 g/m²·a) was notably lower than that of Dushan Lake (63.71 g/m²·a) and Chaohu Lake (40.78 g/m²·a) in eastern China (Duan *et al.*, 2008). Due to the insufficient carbon sink capacity of lakes, the overall carbon sink level of the region was restricted.

3.3. *Spatial-temporal characteristics of land use and carbon emissions*

After applying the classification model to data from different years, the resulting land use classification results were shown on Fig.5. Initially, paddy fields were the predominant land use type in the study area, reflecting long-term land use changes. Land use data from 1990 to 2025 in the demonstration zone were analyzed to estimate carbon emissions over time, utilizing energy consumption data and Eq. 5.

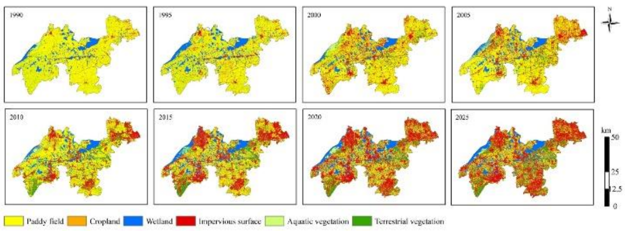

Figure 5. Time series of land use in demonstration zone (1990 ~ 2025)

Based on the results of time series monitoring and wetland area change analysis (Fig.6), the land use evolution process in the demonstration zone can be divided into three stages. During the first stage (1990 ~ 1995), the overall patterns of major landscape types remained stable without significant changes. And the second stage (1995 ~ 2005), urbanization led to a reduction in paddy fields and a slight increase in terrestrial vegetation. By the third stage (2005 ~ 2025), the shrinkage rate of paddy fields accelerated. Urban expansion and human activities jointly served as the main driving factors for landscape evolution during this period, and the coverage area of terrestrial vegetation also expanded significantly. Following the establishment of the demonstration zone in 2020, strict limitations on the growth of impervious surfaces, resulted in a swift slowdown in urban expansion.

Over the entire study period (1990 ~ 2025), the area of paddy fields decreased substantially, with a reduction rate of 68.47 %. The distribution range of natural wetlands did not change significantly throughout the study period, indicating that the development of the demonstration zone did not cause obvious encroachment on natural wetlands. In the areas surrounding wetlands, human activities promoted the construction of ecological protection facilities. These facilities effectively restricted the natural evolution of natural wetlands and largely maintained. In the demonstration zone, the impervious surface showed a rapid expansion trend, with its area increasing nearly sixfold. The primary factor for this change was the expansion of urban land and the construction of roads. Regarding terrestrial vegetation, its distribution evolved from a sporadic state in 1990 to large-scale coverage by 2025. This expansion reflects notable achievements in ecological protection and vegetation restoration in the region.

The areas of all land use types within the demonstration zone, along with their corresponding total carbon emissions, are presented in **Table 6**. Changes in land use directly and significantly affect regional carbon emissions. Throughout the study period, carbon emissions, both total and net, in the demonstration zone increased significantly. From the perspective of temporal characteristics, the contribution of impervious surfaces to carbon emissions has consistently held a dominant position. According to carbon accounting results by land-use type, total carbon emissions in the demonstration zone increased 7.6-fold during the study period. The reduction in carbon emissions is significantly linked to the decline in paddy field area from 1990 to 2025, with emissions decreasing from 3.24×10^4 t to 1.02×10^4 t. Terrestrial vegetation serves as the primary carbon sink in the demonstration zone. Over the same time frame, regional carbon sink rose by 681.44 %, primarily driven by a 93.37 % enhancement in terrestrial vegetation's carbon sink capacity, with the rest attributed to a modest expansion of natural wetlands.

Table 6 Comparison of land use and carbon emissions in demonstration zone (1990 vs. 2025)

		Water	Paddy	Cropland	Impervious	Aquatic vegetation	Terrestrial vegetation
Area/m2	1990	1.15×108	1.97×109	4.67×106	1.89×108	1.31×108	4.36×106
	2025	2.50×108	6.25×108	2.24×107	9.4×108	9.82×107	4.79×108
CE/t	1990	-1936.14	32396.23	232.1495	7.71×105	-2195.46	-253.4824
	2025	-4204.9	10273	1113.593	3.83×106	-1651.7	-27839.57
Rate of change (Based on the results-1990)	217.18 %	31.71 %	479.69 %	496.69 %	75.23 %	10982.84 %	

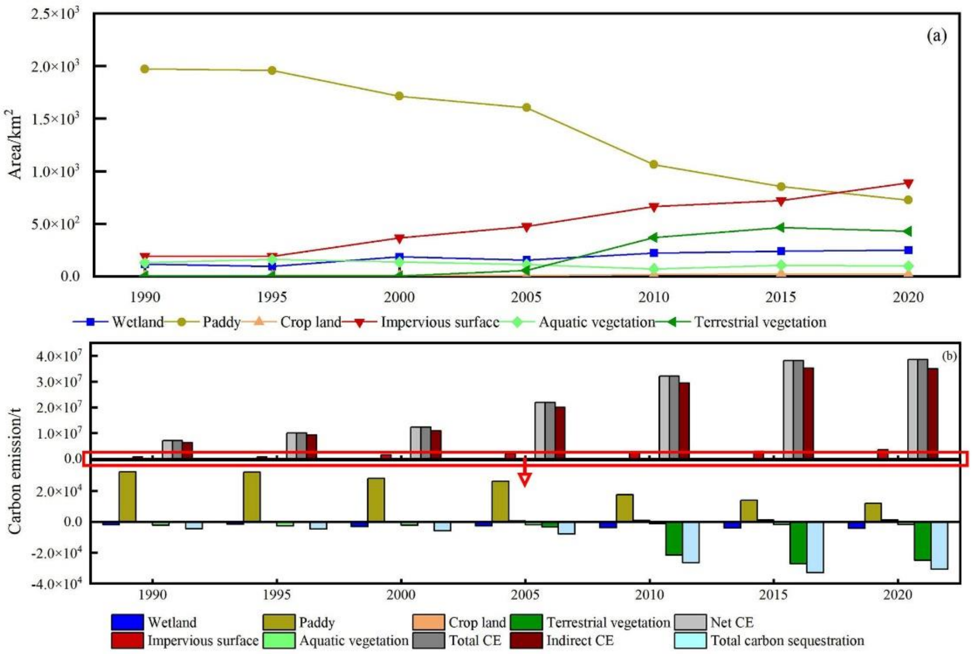

Figure 6. Time series changes of land use and carbon emissions in the demonstration zone from 1990 to 2025 (a: Area change; b: Carbon emission change)

Further analysis indicated that the process of carbon sink change could be divided into two main stages: a relatively gentle phase prior to 2000, followed by a significant and accelerating increase after 2005. This acceleration coincided with the implementation of national ecological restoration policies. Notably, the terrestrial vegetation area in 1990 was extremely small, consisting primarily of paddy fields and cropland. The extensive expansion of plantation forests and ecological restoration efforts between 1990 and 2020 substantially increased this area, contributing to the pronounced enhancement in carbon sequestration capacity observed over the study period.

3.4. *Driving factors of carbon emissions and sustainable development*

3.4.1. Influence of land use transfer on carbon emissions

This study utilised the spatial analysis functions of the ArcGIS platform to overlay the land use classification results of 1990 and 2025, generating a land use transition matrix. Based on this matrix, a diagram of land use type transformation relationships for the corresponding periods was drawn (Fig.7). Between 1990 and 2025, a total of 26 types of land use transition pathways were identified in the demonstration zone. Among them, 11 types were not shown in Fig.6 due to their relatively small transition areas (less than 1 km²).

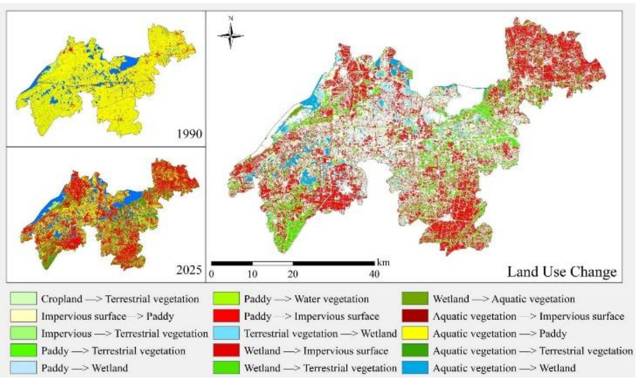

Figure 7. Land use transfer direction in the demonstration zone from 1990 to 2025

In the demonstration zone, paddy fields, the predominant land use type in 1990, primarily converted to impervious surfaces and terrestrial vegetation, with transition areas of 791.02 km² and 473.64 km², respectively. Paddy fields and natural wetlands exhibited notable mutual transformation, covering an area of 1356.57 km², highlighting their dynamic and alternating characteristics. Conversely, a significant bidirectional transformation occurred between aquatic vegetation and open water bodies. However, overall, the transformation was mainly from aquatic vegetation to water bodies, with a net reduction in area of approximately 33.94 km², which may be related to factors such as hydrological regulation, wetland degradation, or artificial dredging.

By 2025, impervious surfaces became the predominant land use in the demonstration zone, primarily due to the urbanization-driven conversion of paddy fields. The area of natural wetlands converted to impervious surfaces was relatively small, and this type of conversion might be related to the construction of tourism and leisure facilities in the demonstration zone (Furgala-Selezniow *et al.*, 2021). During the study period, the spatial pattern of natural wetlands remained stable, whereas notable conversions occurred among paddy fields, terrestrial vegetation, and impervious surfaces. The overall evolutionary trend in the demonstration zone was characterised by the conversion of paddy fields mainly to terrestrial vegetation and impervious surfaces, as well as the transition of aquatic vegetation to open water bodies (Figures 5 and 6).

Among them, the conversion of paddy fields to terrestrial vegetation helps enhance the regional carbon-sequestration capacity. Although the conversion of paddy fields to impervious surfaces may reduce their original direct carbon emissions (such as CH_4 emissions during rice cultivation), impervious surfaces typically correspond to urban, industrial, and transportation land uses. An increase in impervious surfaces will increase energy consumption, leading to more indirect carbon emissions and ultimately having a complex impact on the regional carbon balance.

3.4.2. Driving Effect of Other Factors on Carbon Emissions

In addition to the impact of direct land use type transitions on carbon emissions, this study further analyzed how other potential factors, driven by land use changes, contribute to regional carbon emissions. Based on the multiple collinearity analysis between the net carbon emissions of the demonstration zone and various potential driving factors, which was conducted using Equation 6 and Equation 7 (**Table 7**), only factors without collinearity were considered for analysis. Consequently, parameters such as *GDP, PSI, WA*, and *TPR* were selected to evaluate their impacts on carbon emissions in the demonstration zone. The results are **presented in Figure 8**.

Based on the screened driving factors, after being applied in this study, Eq. 8 and 9 are presented as follows:

$$C = \frac{C}{WA} \times \frac{WA}{PSI} \times \frac{PSI}{GDP} \times \frac{GDP}{TPR} \times TRP \\ = CE_1 \times CE_2 \times CE_3 \times CE_4 \times CE_5 \tag{10}$$

$CE_1 = C/WA$ represents the carbon sink pressure (i.e., the net emissions per unit of wetland area, reflecting the burden on the ecological sink); $CE_2=WA/PSI$ represents the industrial-ecological balance (i.e., the wetland area per unit of secondary industry output, indicating the trade-off between industrial development and wetland conservation); $CE_3=PS/GDPI$ represents the economic structure (the share of secondary industry in the total economy); $CE_4=GDP/TPR$ represents economic development (per capita GDP, a proxy for affluence and consumption-driven emissions); $CE_5=TPR$ represents the total regional population (a scale effect).

$$\Delta C = \Delta C^t - \Delta C^0 = \Delta CE_1 + \Delta CE_2 + \Delta CE_3 + \Delta CE_4 + \Delta CE_5 \tag{11}$$

From 1990 to 2025, the primary factors influencing net carbon emissions in the demonstration zone, in order of impact, are economic development, carbon sink pressure, industrial-ecological balance, total regional population, and economic structure. Between 1990 and 2000, driven by government development policies, economic growth was prioritised in the demonstration zone, resulting in increased carbon sink pressure. Despite the implementation of the Environmental Protection Law in 1994, the absence of complementary land-intensive use policies maintained a significant positive correlation between net carbon emissions and economic growth.

After 2000, with China's accession to the WTO, the secondary industry in the demonstration zone expanded rapidly, and the energy demand for economic development increased significantly. As a result, the contribution of economic factors to net carbon emissions continued to strengthen, and this trend was particularly evident after 2015. However, the carbon emissions growth driven by economic development may have produced a certain policy-offsetting effect with the implementation of the Renewable Energy Law in 2005.The decline in the secondary industry's share within the economic structure has positively contributed to reducing net carbon emissions in the demonstration zone through industrial structure optimization. During the study period, carbon sink pressure consistently positively influenced net carbon emissions, suggesting that the current wetland area or its carbon sink capacity in the demonstration zone may be inadequate to counterbalance the swiftly increasing carbon emissions pressure.

Table 7. Collinearity analysis of factors driving carbon emissions

Factors affecting	*GDP*	*SIO*	*PSI*	*EC*	*CLA*	*WA*	*TVA*	*TCE*	*TRP*
VIF	4.6	5.5	4.0	9.9	337.1	2.8	6.6	24.1	2.6

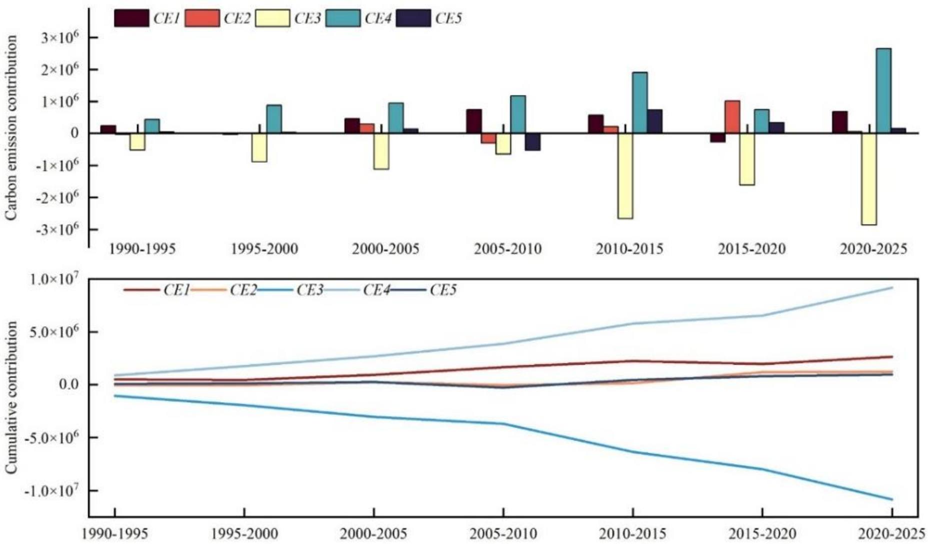

Figure 8. Effect analysis of the driving factors of LMDI in the demonstration zone.

4. Discussion

4.1. *LMDI and economic development of demonstration zone*

This study has established a relatively complete analytical pathway that links land-use classification quality, carbon emission accounting, and driving factor decomposition, with a collinearity pre-screening step introduced before decomposition. Unlike most studies that treat these steps separately, we performed collinearity tests on all candidate variables (Han *et al.*, 2022; Ming *et al.*, 2025). Only those with low correlation (VIF < 5) were retained in the final LMDI model, which to some extent reduces the bias that may arise from overlapping contributions of different factors (Ming *et al.*, 2025). Furthermore, this study incorporated wetland area as an ecological variable among the retained drivers (Tang *et al.*, 2016), thereby extending the analysis beyond economic and demographic indicators. By examining the interrelationship between wetland conservation and urban development constraints, the findings help address the relatively weak assessment of ecological factors in previous land-use carbon emission studies. Our results indicate that, even when ecological variables are controlled for, economic development remains the dominant positive driving factor. Meanwhile, adjustments in economic structure (such as a declining share of secondary industry) can offset emission growth to a certain extent.

Among the multiple factors affecting carbon emissions in the demonstration zone, the interaction between economic growth and ecological degradation provides a critical mechanism underlying the persistent dominance of economic drivers. In the early stage of the study period, industrial expansion under rapid economic growth directly accelerated the conversion of land to built-up and industrial uses. This transformation not only diminished the total area available for natural carbon sequestration but also fragmented remaining vegetation patches, thereby reducing their carbon sink efficiency (Wang *et al.*, 2025). On the other hand, the loss of carbon sinks exacerbated the net emission level (Nzabarinda *et al.*, 2025) and further strengthened the positive contribution of economic factors in the LMDI decomposition. This interaction explains why economic factors remained the dominant driver throughout the study period, despite occasional policy interventions such as the *Renewable Energy Law*. It should be acknowledged that the finding that economic development is the dominant driver of carbon emissions is consistent with previous work in the region (e.g., Sun *et al.*, 2021; Han *et al.*, 2022). The inclusion of wetland area as a screened ecological driver reveals that, even when ecological factors are explicitly modelled, economic factors maintain their primacy—a finding that reinforces the urgency of aligning economic planning with ecological restoration targets, and that provides quantitative support for the demonstration zone's policy goal of balancing development with environmental protection.

4.2. *Classification model and uncertainty analysis of carbon emission data*

The classification model transferability is primarily influenced by spectral differences between Landsat 5 TM and Landsat 8 OLI sensors, as well as by phenological variations in the image acquisition months. Consistent with the findings of most studies, residual biases persist even when radiometrically calibrated and atmospherically corrected satellite data are used (Zhao *et al.*, 2018). Particularly for aquatic vegetation and paddy fields, growth condition differences typically cause inter-annual variations in reflectance because the time window cannot be entirely fixed (Susaki *et al.*, 2004). The BPNN optimisation module within the research framework partly reduces these biases but cannot fully eliminate them. Over long-term trend analyses (multi-decadal scales), these uncertainties are unlikely to overturn the main conclusions, although they may influence the estimated magnitude in specific transitional zones. Future work could incorporate data with better temporal continuity or adopt domain adaptation techniques to further improve cross-sensor consistency. Several factors in the carbon emission estimation process may affect the accuracy of the estimates. The values used (e.g., -0.0581 kg/m²·a for terrestrial vegetation) are spatial averages and may fail to capture local heterogeneity in soil organic carbon, hydrological regimes, or agricultural practices. For example, the carbon sink rate of lakes in the Taihu Basin (16.82 g/m²·a) is notably lower than that of Dushan Lake (63.71 g/m²·a) and Chaohu Lake (40.78 g/m²·a), highlighting the regional variability. In highly urbanised areas, direct carbon emissions are typically much lower than indirect emissions (Andrade *et al.*, 2018); therefore, the estimates can, to a certain extent, represent the actual emissions. Furthermore, as in most current studies, this study assumes equal emission intensity per unit area for all impervious surfaces, ignoring differences in building density, industrial composition, and traffic volume. Research that considers the spatial heterogeneity of carbon emissions remains at an exploratory stage (Wang *et al.*, 2020). Future studies could adopt dynamic emission factors that are linked to remote-sensing-based vegetation productivity and energy consumption statistics at finer spatial scales to reduce this uncertainty. Notwithstanding the uncertainties acknowledged above, the principal contribution of the methodological framework presented in this study resides in its capacity to generate robust relative emission trends and hierarchically ranked driver influences, derived from a fully consistent and harmonised analytical approach applied across the entire 30-year study period. In contrast to cross-sectional investigations confined to narrow temporal windows, this long-term time-series design, underpinned by a unified methodology, affords a more empirically substantiated foundation for the formulation of targeted low-carbon land management policy recommendations.

4.3. *Carbon emissions and environmental changes in demonstration zone*

The "dual carbon" strategy has positioned carbon balance as a crucial metric for evaluating a region's sustainable development potential. In the demonstration zone, wetlands and terrestrial vegetation are the main land use types that carry natural carbon sink potential. Wetlands exhibit a distinct carbon sink capacity compared to terrestrial vegetation, which continuously sequesters carbon as it grows. It is highly susceptible to the quality conditions of wetlands, resulting in significant volatility. And it should be noted that the empirical findings of this study are derived from the specific context of the YRD Demonstration Zone, which encompasses parts of the Taihu Lake Basin. While the analytical framework is transferable, the quantitative results reflect the region's unique land-use composition, policy environment and developmental trajectory.

Land use data indicates that the coverage of aquatic vegetation along the shore of Dianshan Lake significantly decreased between 2005 and 2010, reflecting obvious human interference with the wetland structure. The case of the Taihu Lake Basin further illustrates the complexity of long-term environmental changes. Between 1990 and 2000, water quality continued to deteriorate, mainly due to the increase in industrial wastewater discharge and insufficient pollution control capacity. At the same time, the transformation of agricultural models and the acceleration of urbanization also served as significant driving forces (Lin, 2002). Since 2005, the water quality of wetlands in the demonstration zone has gradually improved (Zhu *et al.*, 2021), which may be related to the strengthening of water pollution control and emission restriction measures.

A study on Dianshan Lake noted a decline in total nitrogen and phosphorus levels after peaking in 2007, attributed to the removal of aquaculture facilities initiated in 2004 (Xiong *et al.*, 2017). Despite this partial recovery in wetland quality, the preceding severe degradation left the ecosystem's carbon sequestration capacity insufficient to offset the sustained rise in regional carbon emissions. This indicates that there is a gap between the current wetland area situation in the demonstration zone and the goal of expanding the wetland area proposed in the Industrial Development Plan for the demonstration zone (2021 ~ 2035). In further research, the demonstration zone should continue prioritising the influence of land-use dynamics on carbon emissions within its sustainable development framework, while intensifying research on the carbon sink mechanisms of wetland ecosystems. Particular attention should be paid to monitoring the efficiency and stability of carbon sink functions across different restoration stages. Moreover, it is essential to identify the key ecological thresholds that affect carbon sequestration capacity and to foster the establishment of a coordinated governance system to support the development of a "carbon sink economy".

5. Conclusions

This study utilised multi-year time-series remote sensing images to analyze the characteristics of land-use patterns and carbon emission changes in the demonstration zone and conducted an in-depth exploration of the relationship between carbon emission changes and their driving factors. The main findings are as follows:

(1) The classification model was developed by employing machine-learning algorithms based on Landsat data. The classification accuracy of the model was 0.93, and the multi-year average accuracy after transfer application was 0.91. By utilizing the classification model, the land-use in the demonstration zone from 1990 to 2025 was obtained. During the study period, the main transformation pathways of land use types in the demonstration zone were as follows: the continuous conversion of paddy fields into terrestrial vegetation areas and impervious surfaces, as well as the mutual transformation between aquatic vegetation and wetlands. (2) From 1990 to 2025, both carbon sinks and carbon sources in the demonstration zone exhibited a significantly increasing trend. The overall carbon balance exhibited characteristics indicative of carbon emissions, with the carbon-source effect being dominant. During the study period, the carbon sink capacity increased by 681.44 %, with the increase in terrestrial vegetation carbon sink capacity contributing 93.37 % to this growth. (3) Land use changes had a potential impact on the net carbon emissions of the demonstration zone during its development process. After conducting multicollinearity analysis and LMDI factor analysis, the impact intensity of each driving factor on net carbon emissions was as follows: economic development > carbon sink pressure > industrial-ecological balance > total regional population > economic structure. Meanwhile, the optimization of the economic structure and industrial restructuring played a positive role in reducing net carbon emissions in the demonstration zone.

Data availability

Data is available on request

Disclosure statement

No potential conflict of interest was reported by the author(s).

Large language model declaration

AI-assisted tools were used solely for language polishing, and all scientific content was authored and carefully verified by the authors.

Funding

This work was supported by the Natural Science Basic Research Program of Shaanxi [grant number (No. 2026JC-YBQN-0350)].

References

Andrade J C S, Dameno A, Pérez J, *et al.* (2018). Implementing city-level carbon accounting: A comparison between Madrid and London. *Journal of cleaner production*, *172*, 795-804.

Aryal J, Sitaula C, & Frery A C. (2023). Land use and land cover (LULC) performance modeling using machine learning algorithms: a case study of the city of Melbourne, Australia. *Scientific reports*, *13*(1), 13510.

Beillouin D, Cardinael R, Berre D, *et al.* (2022). A global overview of studies about land management, land-use change, and climate change effects on soil organic carbon. *Global change biology*, *28*(4), 1690-1702.

Bogale T, Damene S, Seyoum A, *et al.* (2024). A mixed method approach for analyzing drivers of land use land cover change in the Northwestern Ethiopian highlands. *Environmental monitoring and assessment*, *196*(12), 1213.

Cai Z C, Kang G D, Tsuruta H, *et al.* (2005). Estimate of CH4 emissions from year-round flooded rice fields during rice growing season in China. *Pedosphere (Beijing)*, *15*(1), 66-71.

Chaturvedi V, & de Vries W T. (2021). Machine learning algorithms for urban land use planning: A review. *Urban science*, *5*(3), 68.

DeLancey E R, Simms J F, Mahdianpari M, *et al.* (2020). Comparing deep learning and shallow learning for large-scale wetland classification in Alberta, Canada. *Remote sensing*, *12*(1).

Duan X N, Wang X K, Lu F, *et al.* (2008). Carbon sequestration and its potential by wetland ecosystems in China. *Acta ecologica sinica*, *28*(2), 463-469.

Fu B, Zhang L, Xu Z, *et al.* (2015). Ecosystem services in changing land use. *Journal of soils and sediments*, *15*(4), 833-843.

Furgala-Selezniow G, Jankun-Woznicka M, Kruk M, *et al.* (2021). Land use and land cover pattern as a measure of tourism impact on a lakeshore zone. *Land*, *10*(8), Article 787.

Galvanin E A D, Neves S, Cruz C B M, *et al.* (2014). Evaluation of vegetation indexes NDVI, SR and TVI in the discrimination of vegetation types of environments of 'Pantanal' in Caceres, Mato Grosso State. *Ciencia florestal*, *24*(3), 707-715.

Gao B C. (1996). NDWI—A normalized difference water index for remote sensing of vegetation liquid water from space. *Remote sensing of environment*, *58*(3), 257-266.

Gao Y, Zhang N, Ma Q, *et al.* (2024). How is human well-being related to ecosystem services at town and village scales? A case study from the Yangtze River Delta, China. *Landscape ecology*, *39*(7), 126.

Gomes E, Inácio M, Bogdzevič K, *et al.* (2021). Future land-use changes and its impacts on terrestrial ecosystem services: A review. *Science of the total environment*, *781*, 146716.

Han R L, Li L L, Zhang X Y, *et al.* (2022). Spatial-temporal evolution characteristics and decoupling analysis of influencing factors of China's aviation carbon emissions. *Chinese geographical science*, *32*(2), 218-236.

Hou Z, & Liu J. (2024). Enhancing smart grid sustainability: Using advanced hybrid machine learning techniques while considering multiple influencing factors for imputing missing electric load data. *Sustainability*, *16*(18), 8092.

Hou Z, Liu J, & Yu S. (2025). Enhanced analog circuit fault diagnosis via continuous wavelet transform and dual-stream convolutional fusion. *Scientific reports*, *15*(1), 19828.

Huang C, Davis L S, & Townshend J R G. (2010). An assessment of support vector machines for land cover classification. *International journal of remote sensing*, *23*(4), 725-749.

Jia X, Zhang Y, Tan R R, *et al.* (2022). Multi-objective energy planning for China's dual carbon goals. *Sustainable production and consumption*, *34*, 552-564.

Köne A Ç, & Büke T. (2019). Factor analysis of projected carbon dioxide emissions according to the IPCC based sustainable emission scenario in Turkey. *Renewable energy*, *133*, 914-918.

Li N, Lu D S, Wu M, *et al.* (2018). Coastal wetland classification with multiseasonal high-spatial resolution satellite imagery. *International journal of remote sensing*, *39*(23), 8963-8983.

Lin J, Sun D, Zhang Z L, *et al.* (2021). Heavy metals and health risk of rice sampled in Yangtze River Delta, China. *Food additives & contaminants part b-surveillance*, *14*(2), 133-140.

Lin Z. (2002). Analysis of water environmental change in Taihu watershed. *Journal of lake science*, *14*(2), 111-116.

Liu J, Hou Z, Xu Y, *et al.* (2025). Enhanced Beluga Whale optimization meets GRU and adaptive cubature Kalman filter: a novel approach for state of charge estimation in lithium-ion batteries. *Ionics*, *31*(10), 10643-10669.

Lu H, Yang L, Fan Y, *et al.* (2022). Novel simulation of aqueous total nitrogen and phosphorus concentrations in Taihu Lake with machine learning. *Environmental research*, *204*(Pt B), 111940.

Ming X X, Wang Q, Luo K, *et al.* (2025). Multi-scenario carbon emission forecasting through boosting-assisted logarithmic mean divisia index and low emission analysis platform in Zhejiang, China. *Journal of cleaner production*, *537*, Article 147202.

Nzabarinda V, Bao A M, Tie L, *et al.* (2025). Expanding forest carbon sinks to mitigate climate change in Africa. *Renewable & sustainable energy reviews*, *207*, Article 114849.

Ren E, Lin W, Li B, *et al.* (2024). Regional ecological security assessment based on the pressure–state–response framework: The Demonstration Zone of Yangtze River Delta as an example. *Land*, *13*(1), 96.

Shang W, Jin S, He Y, *et al.* (2021). Spatial–temporal variations of total nitrogen and phosphorus in Poyang, Dongting and Taihu Lakes from Landsat-8 data. *Water*, *13*(12).

She X J, Zhang L F, Cen Y, *et al.* (2015). Comparison of the continuity of vegetation indices derived from Landsat 8 OLI and Landsat 7 ETM+ data among different vegetation types. *Remote sensing*, *7*(10), 13485-13506.

Shen C Q, Qian M T, Song Y, *et al.* (2024). Surface pCO2 and air-water CO2 fluxes dominated by submerged aquatic vegetation: Implications for carbon flux in shallow lakes. *Journal of environmental management*, *370*, Article 122839.

Song X P, Hansen M C, Stehman S V, *et al.* (2018). Global land change from 1982 to 2016. *Nature*, *560*(7720), 639-643.

Sun H, Leng Z H, Zhao H S, *et al.* (2021). The impact of air pollution on urban residents' health expenditure: spatial evidence from Yangtze River Delta, China. *Air quality atmosphere and health*, *14*(3), 343-350.

Sun Q, Chen H, Wang Y, *et al.* (2023). Analysis of spatial and temporal carbon emission efficiency in Yangtze River Delta city cluster—Based on nighttime lighting data and machine learning. *Environmental impact assessment review*, *103*, 107232.

Susaki J, Hara K, Park J, *et al.* (2004). Validation of temporal BRDFs of paddy fields estimated from MODIS reflectance data. *IEEE Transactions on geoscience and remote sensing*, *42*(6), 1262-1270.

Tang D C, Ma T Y, Li Z J, *et al.* (2016). Trend prediction and decomposed driving factors of carbon emissions in Jiangsu Province during 2015-2020. *Sustainability*, *8*(10), Article 1018.

Tesfaye A A, & Awoke B G. (2021). Evaluation of the saturation property of vegetation indices derived from sentinel-2 in mixed crop-forest ecosystem. *Spatial information research*, *29*(1), 109-121.

Tian S, Wang S, Bai X, *et al.* (2021). Global patterns and changes of carbon emissions from land use during 1992–2015. *Environmental science and ecotechnology*, *7*, 100108.

Tucker C J. (1979). Red and photographic infrared linear combinations for monitoring vegetation. *Remote sensing of environment*, *8*(2), 127-150.

Wang G, Hu Q, He L, *et al.* (2024). The estimation of building carbon emission using nighttime light images: A comparative study at various spatial scales. *Sustainable cities and society*, *101*, 105066.

Wang G Z, Han Q, & de Vries B. (2020). A geographic carbon emission estimating framework on the city scale. *Journal of cleaner production*, *244*, Article 118793.

Wang J Y, Shao Z F, Fu P, *et al.* (2025). Unraveling the impact of urban expansion on vegetation carbon sequestration capacity: A case study of the Yangtze River Economic Belt. *Sustainable cities and society*, *120*, Article 106157.

Wang P, Luo J, Wan J, *et al.* (2025). The impact of land-use and land-cover change on carbon sink: implications from the case of Guangdong Province, China. *Environmental monitoring and assessment*, *197*(7), 743.

Wu H, Yang Y, & Li W. (2023). Analysis of spatiotemporal evolution characteristics and peak forecast of provincial carbon emissions under the dual carbon goal: Considering nine provinces in the Yellow River basin of China as an example. *Atmospheric pollution research*, *14*(8), 101828.

Xie L, Wang H, & Liu S. (2022). The ecosystem service values simulation and driving force analysis based on land use/land cover: A case study in inland rivers in arid areas of the Aksu River Basin, China. *Ecological indicators*, *138*, 108828.

Xiong G, Wang G, Wang D, *et al.* (2017). Spatio-temporal distribution of total nitrogen and phosphorus in Dianshan lake, China: the external loading and self-purification capability. *Sustainability*, *9*(4), 500.

Zhang C Y, Zhao L, Zhang H, *et al.* (2022). Spatial-temporal characteristics of carbon emissions from land use change in Yellow River Delta region, China. *Ecological indicators*, *136*, 108623.

Zhao Y G, Ma L L, Li C R, *et al.* (2018). Radiometric cross-calibration of Landsat-8/OLI and GF-1/PMS sensors using an instrumented sand site. *IEEE Journal of selected topics in applied earth observations and remote sensing*, *11*(10), 3822-3829.

Zheng H, Peng J, Qiu S, *et al.* (2022). Distinguishing the impacts of land use change in intensity and type on ecosystem services trade-offs. *Journal of environmental management*, *316*, 115206.

Zhu W, Cheng L, Xue Z, *et al.* (2021). Changes of water exchange cycle in Lake Taihu (1986-2018) and its effect on the spatial pattern of water quality. *Journal of lake science*, *33*(4), 1087-1099.